

# Band-selective Holstein polaron in Luttinger liquid material $A_{0.3}\text{MoO}_3$ ( $A = \text{K}, \text{Rb}$ )

L. Kang<sup>1,8</sup>, X. Du<sup>1,8</sup>, J. S. Zhou<sup>1</sup>, X. Gu<sup>1</sup>, Y. J. Chen<sup>1</sup>, R. Z. Xu<sup>1</sup>, Q. Q. Zhang<sup>1</sup>, S. C. Sun<sup>1</sup>, Z. X. Yin<sup>1</sup>, Y. W. Li<sup>2,3</sup>, D. Pei<sup>4</sup>, J. Zhang<sup>2</sup>, R. K. Gu<sup>4</sup>, Z. G. Wang<sup>5</sup>, Z. K. Liu<sup>2,3</sup>, R. Xiong<sup>6</sup>, J. Shi<sup>6</sup>, Y. Zhang<sup>5</sup>, Y. L. Chen<sup>1,2,3,4</sup>✉ & L. X. Yang<sup>1,7</sup>✉

(Quasi-)one-dimensional systems exhibit various fascinating properties such as Luttinger liquid behavior, Peierls transition, novel topological phases, and the accommodation of unique quasiparticles (e.g., spinon, holon, and soliton, etc.). Here we study molybdenum blue bronze  $A_{0.3}\text{MoO}_3$  ( $A = \text{K}, \text{Rb}$ ), a canonical quasi-one-dimensional charge-density-wave material, using laser-based angle-resolved photoemission spectroscopy. Our experiment suggests that the normal phase of  $A_{0.3}\text{MoO}_3$  is a prototypical Luttinger liquid, from which the charge-density-wave emerges with decreasing temperature. Prominently, we observe strong renormalizations of band dispersions, which are recognized as the spectral function of Holstein polaron derived from band-selective electron-phonon coupling in the system. We argue that the strong electron-phonon coupling plays an important role in electronic properties and the charge-density-wave transition in blue bronzes. Our results not only reconcile the long-standing heavy debates on the electronic properties of blue bronzes but also provide a rare platform to study interesting excitations in Luttinger liquid materials.

<sup>1</sup>State Key Laboratory of Low Dimensional Quantum Physics, Department of Physics, Tsinghua University, Beijing 100084, China. <sup>2</sup>School of Physical Science and Technology, ShanghaiTech University and CAS-Shanghai Science Research Center, Shanghai 201210, China. <sup>3</sup>ShanghaiTech Laboratory for Topological Physics, Shanghai 200031, China. <sup>4</sup>Department of Physics, Clarendon Laboratory, University of Oxford, Oxford OX1 3PU, UK. <sup>5</sup>International Center for Quantum Materials, School of Physics, Peking University, Beijing 100871, China. <sup>6</sup>Department of Physics, Wuhan University, Wuhan 430072, China. <sup>7</sup>Frontier Science Center for Quantum Information, Beijing 100084, China. <sup>8</sup>These authors contributed equally: L. Kang, X. Du. ✉email: [yulin.chen@physics.ox.ac.uk](mailto:yulin.chen@physics.ox.ac.uk); [lxyang@tsinghua.edu.cn](mailto:lxyang@tsinghua.edu.cn)

**D**imensional confinement can strongly influence the electronic properties of many-body systems. In drastic contrast to two- or three-dimensional systems, low-energy particle-hole pair in the one-dimensional system can be excited only if its wave vector  $|q| \approx 0$  or  $|q| \approx 2k_F$  with  $k_F$  being the Fermi momentum of electrons (Fig. 1a). The reduction of scattering phase-space and electronic screening gives rise to rich fascinating properties, such as power-law correlation function and spin-charge separated collective bosonic excitations, as properly described by Luttinger liquid (LL) theory<sup>1,2</sup>. On the other hand, quasi-one-dimensional (Q1D) metals with well nested Fermi surface (FS) are highly susceptible toward a charge-density-wave (CDW) state with periodic lattice distortion and an energy gap near  $E_F$  (Fig. 1b)<sup>3</sup>, in which electron-phonon coupling (EPC) usually has a crucial role. Despite the intensive theoretical efforts<sup>4–7</sup>, the LL-to-CDW transition is rarely studied experimentally<sup>8–10</sup>, mainly owing to the lack of a suitable materials platform. Moreover, with stronger EPC, electrons can be dressed by local lattice distortion, forming novel composite quasiparticles—the alleged Holstein polarons that can strongly renormalize the electronic structure of the system and induce energy gaps and “flat bands” at  $-n\Omega_0$  ( $n = 1, 2, \dots$ ) with  $\Omega_0$  being the energy of the strongly coupled phonon involved in the formation of the polaron (Fig. 1c). Up to date, although polarons have been widely observed and well understood in two- or three-dimensional materials<sup>11–16</sup>, they are yet to be discovered in Q1D materials.

On account of the assumptions of LL theory, it is essential for a real material to be a highly anisotropic metal with linear band dispersion. Several crystalline materials meeting these criteria have been demonstrated to be LL candidates, such as 1D cuprate<sup>17</sup>, Lithium purple bronze<sup>18</sup>, Chromium-based superconductor<sup>19</sup>, and organic metallic systems<sup>8,20</sup>. Among the

various Q1D systems, molybdenum blue bronze  $A_{0.3}\text{MoO}_3$  ( $A = \text{K, Rb, Tl}$ ) provides a suitable platform to investigate the LL-to-CDW transition. It exhibits a CDW transition at  $T_{\text{CDW}} \approx 183 \text{ K}$ <sup>21,22</sup> (Supplementary Figure 1), accompanied by a Kohn anomaly<sup>23</sup> and a sharp peak in the Lindhard function<sup>24</sup>. Angle-resolved photoemission spectroscopy (ARPES) measurements suggest an important role of FS nesting in the CDW transition<sup>25,26</sup>. Nevertheless, the absence of the Fermi edge in the density of states<sup>27,28</sup> has challenged this scenario and sparked heavy debates about non-Fermi liquid behavior<sup>29–31</sup> and (pseudo)gap above  $T_{\text{CDW}}$  in the system<sup>25,27,32,33</sup>. Moreover, the underlying microscopic interaction that is crucial for the CDW transition is also under heavy debate<sup>25,26,33,34</sup>. These controversial results call for a comprehensive understanding of the single-particle spectral properties of the system.

In this work, we report a high-resolution laser-based ARPES study of the blue bronze  $A_{0.3}\text{MoO}_3$  ( $A = \text{K, Rb}$ ). By tracking the band dispersion over a wide temperature range, we provide spectroscopic evidence of the CDW transition near  $T_{\text{CDW}} \approx 183 \text{ K}$ . Above  $T_{\text{CDW}}$ , we observe a linear band dispersion with power-law scaling behavior of ARPES spectral weight, which can be precisely described by the LL model<sup>35</sup>. Below  $T_{\text{CDW}}$ , the LL property of the spectra revives after the CDW gap is suppressed by surface doping of Rubidium (Rb) atoms. Interestingly, we observe strong renormalizations of the band dispersions, which are identified as the spectral function of Holstein polaron derived from band-selective EPC in the system. We conclude that the strong EPC<sup>22,34,36,37</sup>, in addition to the FS nesting<sup>25,26</sup>, has an important role in electronic properties and the LL-to-CDW transition in blue bronzes. Our results not only help understand the long-standing mysteries in blue bronzes, including the non-Fermi liquid behavior, the pseudogap above  $T_{\text{CDW}}$ , and the mechanism of the CDW transition but also provide a rare

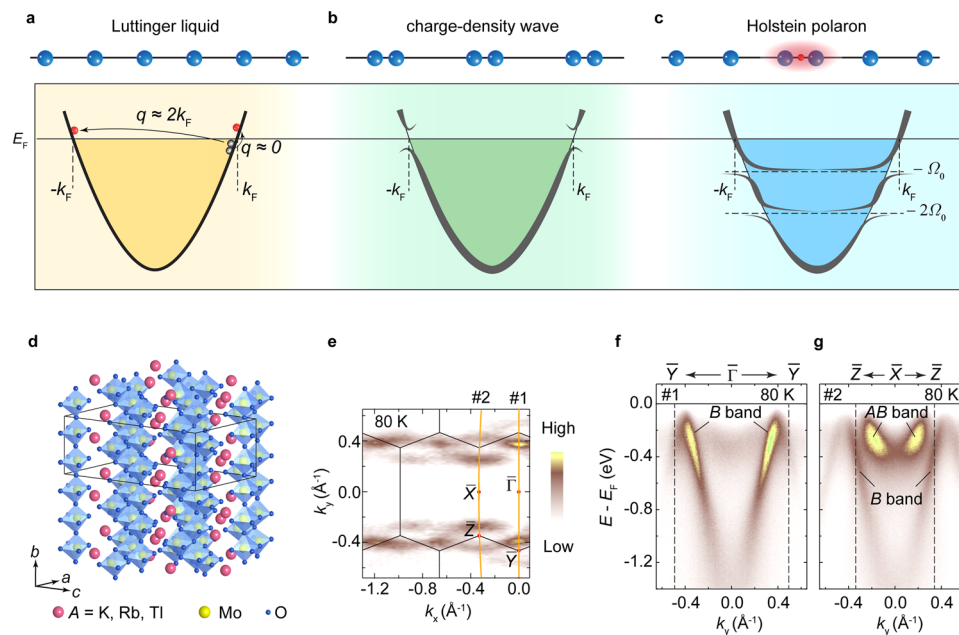


**Fig. 1** Physics in one dimension and basic band structure of  $\text{K}_{0.3}\text{MoO}_3$ . **a** Luttinger liquid (LL) behavior in one dimension, where only low-energy particle-hole pairs with wave vector  $|q| \approx 0$  or  $|q| \approx 2k_F$  can be excited. **b** Charge-density-wave (CDW) and periodic lattice distortion, leading to a gap opening near the Fermi energy ( $E_F$ ). **c** An electron dressed by the local lattice distortion, forming the Holstein polaron and leading to band gaps and flat dispersions near multiples of the phonon energy ( $\Omega_0$ ). **d** Crystal structure of  $A_{0.3}\text{MoO}_3$  ( $A = \text{K, Rb, Tl}$ ) showing one-dimensional chains of  $\text{MoO}_6$  octahedrons. Black lines indicate the unit cell. **e** Experimental Fermi surface (FS) by integrating ARPES intensity in an energy window of 20 meV near the Fermi energy ( $E_F$ ), with surface Brillouin zone appended. **f, g** Band dispersions along and  $\bar{X} - \bar{Z}$  showing the bonding (B) and anti-bonding (AB) bands measured along with cuts #1 and #2 as indicated by the orange lines in **e**. The dashed lines indicate the momentum position of high symmetry points. Data in **e-g** were collected at 80 K with a He lamp ( $h\nu = 21.2 \text{ eV}$ ).

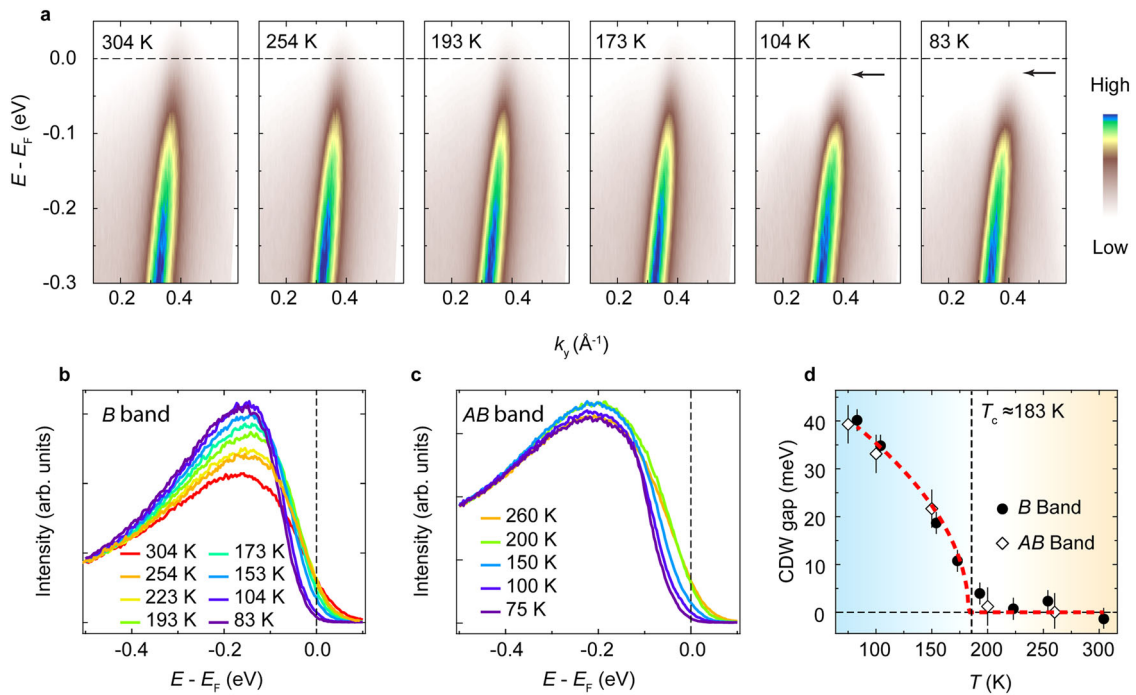


**Fig. 2** CDW transition in  $K_{0.3}MoO_3$ . **a** Temperature evolution of the band dispersion along the  $\bar{\Gamma} - \bar{Y}$  direction. The black arrows indicate the CDW gap opening below  $T_{CDW} \approx 183$  K. The dashed lines indicate  $E_F$ . **b, c** Energy distribution curves (EDCs) near Fermi momenta of *B* (**b**) and *AB* (**c**) bands at different temperatures showing the CDW gap opening below  $T_{CDW}$ . The dashed lines indicate  $E_F$ . **d** CDW gap as a function of temperature. The CDW gap is determined by the shift of the EDC leading edge with respect to the spectrum at high temperatures. The error bars are determined by the combination of energy resolution and deviations between samples. The red dashed line is the fit to the BCS-type gap equation. Data were collected with a linear-horizontally polarized laser at 7 eV.

platform to study the intriguing EPC in LL materials, which will also shed light on the understanding of rich physics in other Q1D materials.

**Results**

**CDW transition in blue bronze.** As shown in Fig. 1d,  $A_{0.3}MoO_3$  crystallizes into the monoclinic structure with space group  $C2/m$ . It consists of 1D chains of  $MoO_6$  octahedrons extending along the [010] direction and  $MoO_3$  layers intercalated by *A* atoms stacking along the [201] direction<sup>38</sup>. Fig. 1e shows the Q1D FSs running perpendicular to  $b^*$  (along  $k_x$ ) measured at 80 K, consistent with the Q1D crystal structure and in good agreement with our calculation (Supplementary Figure 3). Fig. 1f and g show band dispersions along the  $\bar{\Gamma} - \bar{Y}$  and  $\bar{X} - \bar{Z}$  directions. The bonding (*B*) band shows a linear dispersion in a large energy range, whereas the anti-bonding (*AB*) band shows a relatively narrow bandwidth with a band bottom near 370 meV below  $E_F$ , in good agreement with our calculation (Supplementary Figure 4).

To investigate the CDW transition in  $A_{0.3}MoO_3$ , we track the temperature evolution of the band dispersion using laser-based ARPES with superb resolutions, as shown in Fig. 2. At 304 K, we observe a strong suppression of the spectral weight near  $E_F$  and the absence of Fermi edge. With decreasing temperature, the spectral weight is further suppressed and an energy gap ( $\Delta_{CDW}$ ) gradually opens below  $T_{CDW}$ , as also shown by the energy distribution curves (EDCs) near the Fermi momenta  $k_F$  of the *B* and *AB* bands (Fig. 2b, c). The CDW gap is about 42 meV at 83 K (Fig. 2d) and follows the BCS-type gap equation, in accordance with previous reports<sup>27,33,39,40</sup> and the estimation based on our resistivity measurements (Supplementary Figure 1).

**LL nature of the normal state.** As schematically shown in Fig. 3a, the spectral density in LLs shows a power-law behavior near  $E_F$ ,

which can be directly recognized by ARPES<sup>9,18,19,31,41</sup>. In blue bronzes, the absence of Fermi edge was previously attributed either to non-Fermi liquid behavior<sup>30</sup> or the pseudogap induced by the CDW fluctuations<sup>25,27,32,33</sup>. However, compelling evidence for both scenarios is yet to be derived. In Fig. 3b, we approximate the EDCs integrated along  $\bar{\Gamma} - \bar{Y}$  near  $E_F$  with a LL spectral function at finite temperatures<sup>35</sup>:

$$\rho(\epsilon, T) \propto T^\alpha \text{Re} \left[ (2i)^{\alpha+1} \beta \left( \frac{\alpha + 1 + \frac{i\epsilon}{\pi}}{2}, -\alpha \right) \right] \quad (1)$$

where  $\epsilon = (E - E_F)/k_B T$  is the scaled energy,  $\beta$  is the beta function, and  $\alpha$  is the LL anomalous exponent. The EDCs fit perfectly to the LL spectral function convoluted with the energy resolution in our experiment with  $\alpha = 0.6 \pm 0.1$  (Supplementary Figure 5) as shown in Fig. 3b. Moreover, Eq. (1) suggests a scaling relation of the EDCs, that is,  $\rho(\epsilon, T)/T^\alpha$  is independent of the temperature, which is well established in Fig. 3c with the same  $\alpha$ , proving the LL nature of blue bronzes in the normal state.

At temperatures slightly below  $T_{CDW}$ , the spectra still fit nicely to the LL model after introducing an extra fitting parameter  $\Delta$  accounting for the CDW gap in the spectral function (Supplementary Figure 6), suggesting the intimate relationship between the CDW state and the LL phase. Fig. 3d shows the temperature evolution of  $\alpha$ . It increases slightly with decreasing temperature (above  $T_{CDW}$ ), in contrast to the two-band model proposed in  $Li_{0.9}Mo_6O_{17}$ <sup>18,42</sup>. Far below  $T_{CDW}$ , the EDCs cannot be fitted to the LL model owing to the strong modification of the LL phase by the CDW ordering (Supplementary Figure 6). Interestingly, the LL property revives after the CDW gap is suppressed by doping Rb atoms on the sample surface as shown by the shift of the leading edge of the EDCs in Fig. 3e and f, which saturates to a value of about 20 meV (Fig. 3f and Supplementary Figure 7). After that, the spectrum again fits well to the LL model as shown

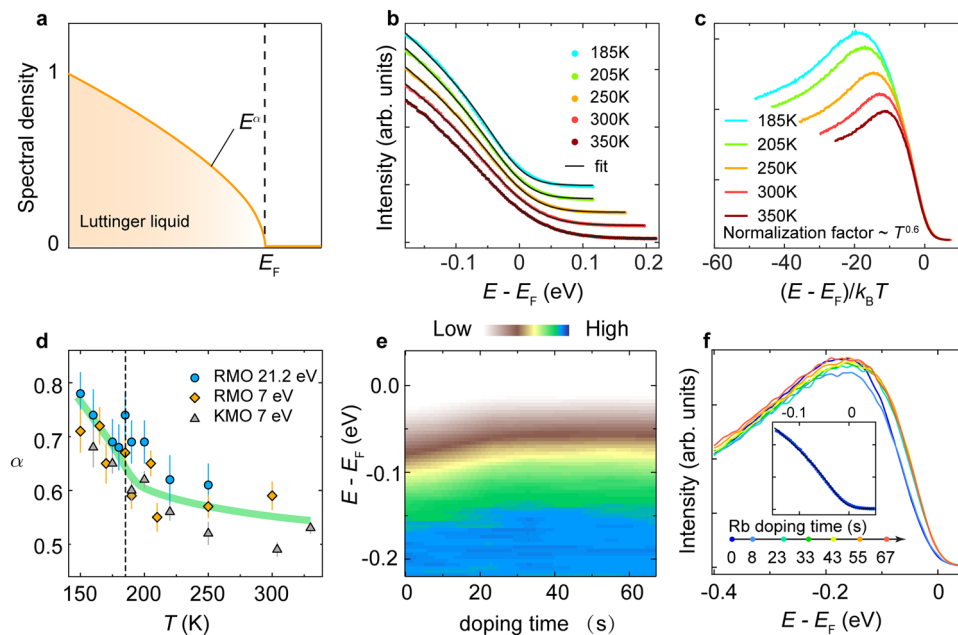


**Fig. 3 Luttinger liquid behavior of  $A_{0.3}MoO_3$ .** **a** The spectral density of LLs (orange curve) showing a power-law dependence on the energy. **b** EDCs of  $Rb_{0.3}MoO_3$  integrated along  $\bar{\Gamma} - \bar{Y}$  with fits to finite temperature LL model (black curves). The curves are vertically offset for clarity. **c** Scaling plot of the EDCs at different temperatures. The scaling factor is  $T^\alpha$  with  $\alpha = 0.6$ . **d** The anomalous exponent  $\alpha$  as a function of temperature measured with He lamp (circles) and laser (diamonds and triangles). The error bars are determined by the combination of the confidence intervals of the data fitting and deviations between samples. **e, f** Evolution of the EDCs near  $k_F$  of the  $B$  band with surface Rb doping. The inset in **f** shows the fit of the integrated EDC after 6th (67 s) Rb doping to the LL model. Data in panels **b** and **c** were collected using 7 eV laser, whereas the data in panels **e** and **f** were collected using He lamp (Supplementary Figure 7).

in the inset of Fig. 3f, further proving our conclusion that the normal state of the blue bronze is a LL.

**Spectral function of Holstein polaron.** To understand the microscopic interactions underlying the LL-to-CDW transition, we perform further spectroscopic analyses in Fig. 4. Fig. 4a shows the ARPES spectrum of the  $AB$  band (left) and its second derivative with respect to the energy (right). Interestingly, we observe a flat band near  $-150$  meV and a discontinuity in the dispersion near  $-170$  meV, which are clearly resolved in the EDCs (Fig. 4b), but absent in the ab initio calculation (Supplementary Note 3) and previous ARPES measurements. For a more-detailed inspection of the spectral function, we approximate the momentum distribution curves (MDCs) of the  $AB$  band with Lorentzians. Despite the strong suppression of the spectral weight by the LL nature of the system, we can still extract the band dispersion and the spectral broadening  $\Delta k(E)$  near  $E_F$ . As shown in Fig. 4c and d, we observe a kink-like structure near  $-85 \pm 10$  meV.

The doubled energy positions of the band renormalizations at  $\approx -85$  meV and  $\approx -170$  meV mimic the characteristic spectral function of Holstein polarons that are usually manifested by a series of band renormalization at  $-n\Omega_0$  ( $n = 1, 2, \dots$ ), where  $\Omega_0$  is the energy of the phonon mode involved in the formation of the polaron (Fig. 1c)<sup>11,13,43</sup>. To verify the formation of Holstein polaron in the blue bronze, we simulate its spectral function by a simple momentum-average model (see Methods for details)<sup>11,43</sup>. Considering the energy position of the kink-like structure and the dispersion discontinuity, we adopt a phonon mode with the energy of  $\approx 85$  meV in the simulation<sup>44,45</sup>. Fig. 4e–g elucidate the evolution of the band renormalizations with increasing EPC parameter  $\lambda$ . At  $\lambda \approx 0.6$  (Fig. 4g), both the flat band and the kink-like structure are excellently reproduced by our simple approximation (also see the EDCs of the simulated spectrum in Fig. 4h),

confirming the formation of Holstein polaron in the system. It is noteworthy that the band renormalization near  $-85$  meV is concealed by the suppression of the spectral weight near  $E_F$  and is instead manifested by a kink-like structure in our experiment and simulation.

## Discussion

Although the electronic properties are radically different in Fermi liquids and LLs, we observe the formation of Holstein polaron in a LL material, similar to that in Fermi liquids<sup>11</sup>. To understand the mechanism of Holstein polaron in blue bronzes, it is crucial to reveal the nature of the phonon mode involved. The phonon mode at  $\approx 85$  meV is identified as the bridge Mo-O-Mo stretching mode as observed in Raman scattering and infrared spectroscopic experiments<sup>44,45</sup>. Owing to the Q1D crystal structure of blue bronzes, this phonon mode is spatially localized perpendicular to the atomic chains, thus is short-range in nature. Along the atomic chains, however, it can be relatively extended. The size or the coherence length of the Holstein polaron can be estimated by  $l = \tau v_p$ , where  $\tau$  and  $v_p$  are the lifetime and velocity of the quasiparticles.  $\tau$  and  $v_p$  can be obtained from the spectral broadening and Fermi velocity of the  $AB$  band, respectively. With  $v_p \approx 3$  eV  $\text{\AA}$  and MDC width  $\Delta k = 0.12$   $\text{\AA}^{-1}$  near  $E_F$ , we estimate  $\tau \approx 11$  fs and thus  $l \approx 8.3$   $\text{\AA}$ , slightly larger than the lattice constant along the atomic chains.

Moreover, the strong band renormalizations and the formation of Holstein polaron are absent in the  $B$  band and the  $AB$  band is much more broadened than the  $B$  band, suggesting an interesting band-selective EPC. It is very likely that the phonon mode at  $\approx 85$  meV involves mainly the Mo II atoms whose orbitals contribute significantly to the  $AB$  band (Supplementary Note 3), giving rise to the band-selective formation of Holstein polarons. Even so, the  $B$  band is also influenced by the strong EPC in the system. By quantitative analyses, we show that the electron self-

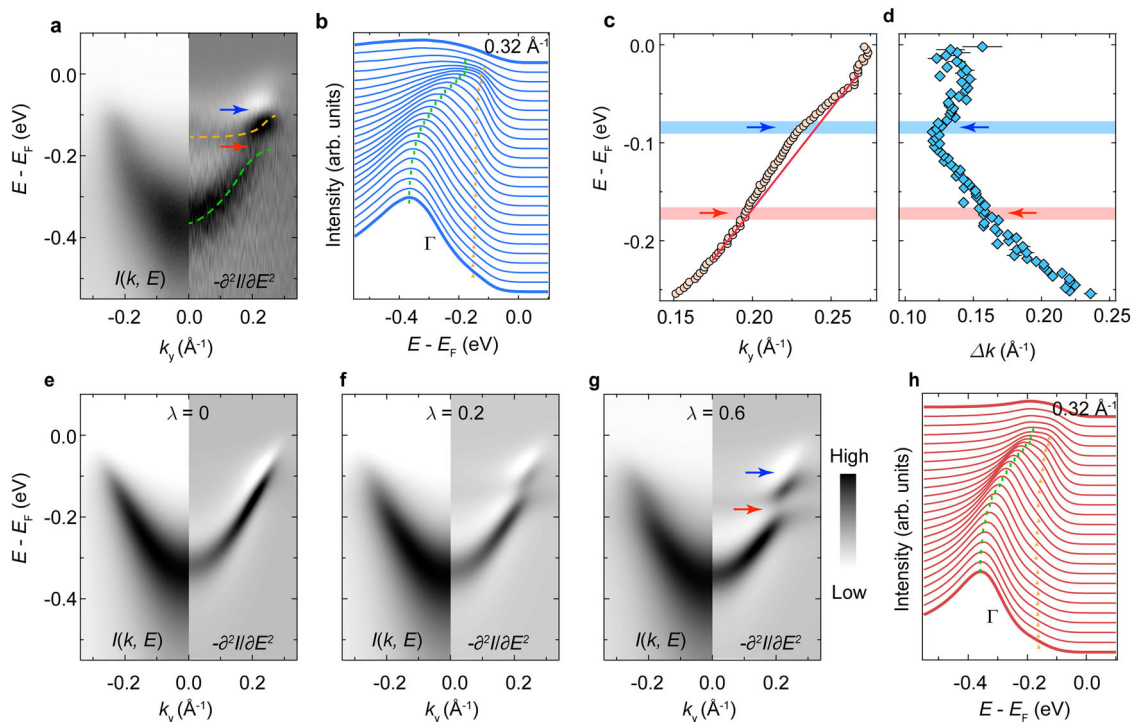


**Fig. 4 Holstein polarons in  $\text{K}_{0.3}\text{MoO}_3$ .** **a** ARPES intensity map of the AB band along  $\bar{X} - \bar{Z}$  (left) and its second derivative (right) with respect to the energy axis measured with linear-vertically polarized 7 eV laser at 75 K. The orange and green dashed curves are the guides to the eyes for the band discontinuity (emphasized with blue and red arrows). **b** Stacking plot of EDCs showing observed dispersions. The green bar and orange triangles are the guides to the eyes for dispersions. **c, d** Extracted AB band dispersion (**c**) and the spectral broadening (**d**) showing a kink-like feature near 85 meV below  $E_F$  (blue arrow). The red line in panel **c** is the guide to eyes for the bare band dispersion. The error bars are determined by the combination of the confidence intervals of the data fitting and deviations between samples. **e-g** Simulation of the spectral function (left) and its second derivative (right) of Holstein polarons at different EPC parameters. **h** Simulated EDCs showing good agreement with the raw data in **a**. The green bar and orange triangles are the guides to the eyes for dispersions.

energy of the B band near  $E_F$  strongly depends on the temperature (Supplementary Note 8), further confirming the strong EPC in blue bronzes<sup>22,34,36,37</sup>. Likewise, the estimated coherence length of the Holstein polaron is in good comparison with the CDW period of  $\sim 9 \text{ \AA}$ , and the phonon mode involved in the Holstein polaron is intimately related to the CDW transition<sup>35,44,45</sup>, suggesting that the strong EPC and its band-selectivity may play an important role in the electronic properties and the LL-to-CDW transition in blue bronzes.

It is worth noting that we do not observe clear evidence of spin-charge separation, although it has been suggested in some previous ARPES measurements<sup>26</sup>. Although the spin-charge separation is evidenced in a few LL materials<sup>17,20,46</sup>, it is difficult to observe in the blue bronze: On the one hand, the LL phase is only well established in blue bronzes at high temperatures where the strong thermal fluctuation challenges the observation of spin-charge separation. On the other hand, the dispersions of the separated spinon and chargin are expected to be well resolvable only in LL materials with  $\alpha$  much smaller than 0.5<sup>19,31</sup>. For example, it is likewise absent in the prototypical LL material  $\text{Li}_{0.9}\text{Mo}_6\text{O}_{17}$  with a similar value of  $\alpha = 0.65$ <sup>18</sup>. Finally but also importantly, the strong EPC may smear the spin-charge separation in the system by strongly broadening the dispersion of the chargin and reducing its spectral weight<sup>47,48</sup>.

In summary, using high-resolution laser-based ARPES, we systematically investigate the electronic structure of blue bronze. Our results indicate a LL phase of the system in the normal state. We observe Holstein polarons that strongly renormalize the band dispersion. We, therefore, conclude that the strong EPC has an important role in the spectral properties and CDW transition of

blue bronzes. Our work suggests that the physics in blue bronze may be properly described by the 1D Holstein model, in which EPC is a vital parameter in the phase diagram<sup>7</sup>.

## Methods

**Sample preparation.** The  $\text{A}_{0.3}\text{MoO}_3$  single crystals were grown by an electrolytic reduction method<sup>49</sup>.  $\text{A}_2\text{CO}_3$  (99.5% purity) and  $\text{MoO}_3$  (99% purity) were used as reagent materials in standard electrolysis run with a molar ratio of 1:4.3. During a typical run, the furnace temperature is increased to 600°C for 40 min and maintained for 2 h. Then the temperature was brought tardily (1°C/min) to 5–10 °C above the solidification temperature of the liquid of  $\text{A}_2\text{CO}_3$  and  $\text{MoO}_3$  mixture. A current of 25 mA was applied through the melt during the electrolytic process and maintained for 2–2.5 h. This process of crystal growth can be repeated many times during several days, after which platelet crystals were obtained.

**ARPES.** High-resolution ARPES measurements were performed at beamline 13U of National Synchrotron Radiation Laboratory (NSRL), China, beamline 9 A of Hiroshima Synchrotron Radiation Center (HSRC), Japan, and Peking University, China. Data were collected with Scienta R4000 (DA30) electron analyzers at NSRL and HSRC (Peking University). The overall energy and angle resolutions were set to 15 meV and 0.2°, respectively.

**Laser-based ARPES.** Laser-based ARPES measurements were performed using DA30L analyzers and vacuum ultraviolet 7 eV lasers in Tsinghua University and ShanghaiTech University, China. The overall energy and angle resolutions were set to 6 meV and 0.2°, respectively. The samples were cleaved in situ and measured under ultra-high vacuum below  $1.0 \times 10^{-10}$  mbar. Surface Rb doping was performed in situ at 80 K using a SAES alkali-metal source after well outgassing. The current was set to 5.6 A.

**Single-crystal X-ray diffraction.** Single-crystal XRD was performed using Mo target by the Rigaku Oxford Diffraction at the Department of Physics, University of Oxford. The beam spot size is 10–200  $\mu\text{m}$  in diameter. The data were collected and analyzed by the CrysAlisPro software.

**Transport measurement.** Transport measurements were taken in the Physical Properties Measurement System of Quantum Design.

**First-principles calculation.** Electronic structure calculations were performed using density functional theory<sup>50</sup> with the projected augmented wave method as implemented in the QUANTUM ESPRESSO package<sup>51,52</sup>. The exchange-correlation functional was approximated within the Perdew–Burke–Ernzerhof scheme<sup>53</sup>. Experimental structural parameters were relaxed with a force threshold of 0.01 eV/Å. The cutoff energy for the plane-wave basis was set to 600 eV and the Monkhorst-Pack k-point mesh of  $9 \times 9 \times 9$  was used to get a self-consistent charge density. The FS was calculated with a denser mesh of  $16 \times 16 \times 16$  and checked by the tight-binding-based calculation supplied by the Wannier90 code<sup>54</sup>.

**Simulation of the spectral function of Holstein polaron.** The spectral function calculation of Holstein polaron is performed within momentum-average approximation<sup>43</sup>, which is demonstrated to feature high efficiency and accuracy<sup>11,43</sup>. The model has a simple form of an electron coupled with a dispersionless phonon mode, i.e., Holstein polaron. The Green's function of the Holstein model is represented as:

$$G(\mathbf{k}, \omega) = \frac{1}{\omega - \epsilon_{\mathbf{k}} - \Sigma_{\text{MA}}(\omega) + i\eta} \quad (2)$$

where  $\omega$  is the energy,  $\epsilon_{\mathbf{k}}$  is the bare dispersion,  $\eta$  is the spectral broadening parameter, and the momentum-averaged self-energy  $\Sigma_{\text{MA}}(\omega)$  has simple analytic form for 1D systems:

$$\Sigma_{\text{MA}}(\omega) = \frac{g^2 \Omega_0 \bar{g}_0(\omega - \Omega_0)}{1 - \frac{2g^2 \bar{g}_0(\omega - \Omega_0) \bar{g}_0(\omega - 2\Omega_0)}{1 - \frac{3g^2 \bar{g}_0(\omega - 2\Omega_0) \bar{g}_0(\omega - 3\Omega_0)}{1 - \dots}}} \quad (3)$$

$$\bar{g}_0(\omega) = \frac{\text{sgn}(\omega)}{\sqrt{(\omega + i\eta)^2 - 4t^2}} \quad (4)$$

where  $\Omega_0$  is the energy of the phonon involved in the formation of Holstein polarons,  $g^2$  is related to EPC constant  $\lambda$  by  $g^2 = 2t\Omega_0\lambda$  and  $t$  is the hopping amplitude.

In the spectral function simulation, the quadratic energy dependence of  $\eta$  is adopted and a LL type spectral weight is included to mimic the experimental spectral function of AB band.

## Data availability

The data sets that support the findings of this study are available from the corresponding author upon reasonable request.

Received: 4 May 2021; Accepted: 14 September 2021;

Published online: 26 October 2021

## References

- Giamarchi T. *Quantum physics in one dimension*. Clarendon Press (2003).
- Haldane, F. D. M. 'Luttinger liquid theory' of one-dimensional quantum fluids. I. Properties of the Luttinger model and their extension to the general 1D interacting spinless Fermi gas. *J. Phys. C Solid State Phys.* **14**, 2585–2609 (1981).
- Gruber G. *Density Waves in Solids*. (Perseus Publishing, 1994).
- Hohenadler, M., Wellein, G., Bishop, A. R., Alvermann, A. & Fehske, H. Spectral signatures of the Luttinger liquid to the charge-density-wave transition. *Phys. Rev. B* **73**, 245120 (2006).
- Ejima, S., Hager, G. & Fehske, H. Quantum phase transition in a 1D transport model with Boson-affected hopping: luttinger liquid versus charge-density-wave behavior. *Phys. Rev. Lett.* **102**, 106404 (2009).
- Hohenadler, M., Assaad, F. F. & Fehske, H. Effect of electron-phonon interaction range for a half-filled band in one dimension. *Phys. Rev. Lett.* **109**, 116407 (2012).
- Bursill, R. J., McKenzie, R. H. & Hamer, C. J. Phase diagram of the one-dimensional holstein model of spinless fermions. *Phys. Rev. Lett.* **80**, 5607–5610 (1998).
- Ito, T. et al. Temperature-dependent luttinger surfaces. *Phys. Rev. Lett.* **95**, 246402 (2005).
- Nicholson, C. W. et al. Dimensional crossover in a charge density wave material probed by angle-resolved photoemission spectroscopy. *Phys. Rev. Lett.* **118**, 206401 (2017).
- Mou, D. et al. Discovery of an unconventional charge density wave at the surface of  $\text{K}_{0.9}\text{Mo}_6\text{O}_{17}$ . *Phys. Rev. Lett.* **116**, 196401 (2016).
- Kang, M. et al. Holstein polaron in a valley-degenerate two-dimensional semiconductor. *Nat. Mater.* **17**, 676–680 (2018).
- Chen, C., Avila, J., Frantzeskakis, E., Levy, A. & Asensio, M. C. Observation of a two-dimensional liquid of Fröhlich polarons at the bare  $\text{SrTiO}_3$  surface. *Nat. Commun.* **6**, 8585 (2015).
- Franchini, C., Reticioli, M., Setvin, M. & Diebold, U. Polarons in materials. *Nat. Rev. Mater.* **6**, 560–586 (2021).
- Moser, S. et al. Tunable polaronic conduction in anatase  $\text{TiO}_2$ . *Phys. Rev. Lett.* **110**, 196403 (2013).
- Riley, J. M. et al. Crossover from lattice to plasmonic polarons of a spin-polarised electron gas in ferromagnetic  $\text{EuO}$ . *Nat. Commun.* **9**, 2305 (2018).
- Cancellieri, C. et al. Polaronic metal state at the  $\text{LaAlO}_3/\text{SrTiO}_3$  interface. *Nat. Commun.* **7**, 10386 (2016).
- Kim, B. J. et al. Distinct spinon and holon dispersions in photoemission spectral functions from one-dimensional  $\text{SrCuO}_2$ . *Nat. Phys.* **2**, 397–401 (2006).
- Wang, F. et al. New Luttinger-liquid physics from photoemission on  $\text{Li}_{0.9}\text{Mo}_6\text{O}_{17}$ . *Phys. Rev. Lett.* **96**, 196403 (2006).
- Watson M. D. et al. Multiband one-dimensional electronic structure and spectroscopic signature of tomonaga-luttinger liquid behavior in  $\text{K}_2\text{Cr}_3\text{As}_3$ . *Phys. Rev. Lett.* **118**, 097002 (2017).
- Claessen, R. et al. Spectroscopic signatures of spin-charge separation in the quasi-one-dimensional organic conductor TTF-TCNQ. *Phys. Rev. Lett.* **88**, 096402 (2002).
- Pouget, J. P., Kagoshima, S., Schlenker, C. & Marcus, J. Evidence for a Peierls transition in the blue bronzes  $\text{K}_{0.30}\text{MoO}_3$  and  $\text{Rb}_{0.30}\text{MoO}_3$ . *J. Phys. Lett.* **44**, 113–120 (1983).
- Mankowsky, R. et al. Dynamical stability limit for the charge density wave in  $\text{K}_{0.3}\text{MoO}_3$ . *Phys. Rev. Lett.* **118**, 116402 (2017).
- Pouget, J. P., Hennion, B., Escribe-Filippini, C. & Sato, M. Neutron-scattering investigations of the Kohn anomaly and of the phase and amplitude charge-density-wave excitations of the blue bronze  $\text{K}_{0.3}\text{MoO}_3$ . *Phys. Rev. B* **43**, 8421–8430 (1991).
- Guster, B., Pruneda, M., Ordejón, P., Canadell, E. & Pouget, J.-P. Evidence for the weak coupling scenario of the Peierls transition in the blue bronze. *Phys. Rev. Mat.* **3**, 055001 (2019).
- Ando, H. et al. Angle-resolved photoemission study of  $\text{K}_{0.3}\text{MoO}_3$ : direct observation of temperature-dependent Fermi surface across the Peierls transition. *J. Phys. Condens. Matter* **17**, 4935–4940 (2005).
- Mou, D., Konik, R. M., Tselik, A. M., Zaliznyak, I. & Zhou, X. Charge-density wave and one-dimensional electronic spectra in blue bronze: Incoherent solitons and spin-charge separation. *Phys. Rev. B* **89**, 201116 (2014).
- Dardel, B. et al. Temperature dependence of the spectral function through the peierls transition in quasi-one-dimensional compounds. *Europhys. Lett.* **19**, 525–530 (1992).
- Griioni, M., Perfetti, L. & Berger, H. Strong electron–electron and electron–phonon interactions in one- and two-dimensional solids. *J. Electron Spectros. Relat. Phenom.* **137–140**, 417–423 (2004).
- Allen, J. W. Quasi-particles and their absence in photoemission spectroscopy. *Solid State Commun.* **123**, 469–487 (2002).
- Gweon, G. H. et al. ARPES line shapes in FL and non-FL quasi-low-dimensional inorganic metals. *J. Electron Spectros. Relat. Phenom.* **117–118**, 481–502 (2001).
- Gweon, G. H., Allen, J. W. & Denlinger, J. D. Generalized spectral signatures of electron fractionalization in quasi-one- and two-dimensional molybdenum bronzes and superconducting cuprates. *Phys. Rev. B* **68**, 195117 (2003).
- Tanaka, S., Ueda, E. & Sato, M. STM-STS studies of molybdenum oxides conductors. *Solid State Commun.* **87**, 877–881 (1993).
- Perfetti, L. et al. Mobile small polarons and the Peierls transition in the quasi-one-dimensional conductor  $\text{K}_{0.3}\text{MoO}_3$ . *Phys. Rev. B* **66**, 075107 (2002).
- Yang, L. X. et al. Bypassing the structural bottleneck in the ultrafast melting of electronic order. *Phys. Rev. Lett.* **125**, 266402 (2020).
- Orgad, D. Spectral functions for the tomonaga-luttinger and luther-emery liquids. *Philos. Mag. B* **81**, 377–398 (2001).
- Degiori, L. et al. Fluctuation effects in quasi-one-dimensional conductors: optical probing of thermal lattice fluctuations. *Phys. Rev. B* **52**, 5603–5610 (1995).
- Beyer, R., Barišić, N. & Dressel, M. Charge-density fluctuations probed by vibronic modes of  $\text{K}_{0.3}\text{MoO}_3$ . *Phys. B Condens. Matter* **407**, 1823–1826 (2012).
- Graham, J. & Wadsley, A. D. The crystal structure of the blue potassium molybdenum bronze,  $\text{K}_{0.28}\text{MoO}_3$ . *Acta Crystallogr.* **20**, 93–100 (1966).
- Brutting, W. & Nguyen, P. H. Rie beta W, Paasch G. DC-conduction mechanism and Peierls gap in organic and inorganic charge-density-wave conductors. *Phys. Rev. B* **51**, 9533–9543 (1995).
- Schwartz, A. et al. Fluctuation effects on the electrostatics of quasi-one-dimensional conductors above the charge-density-wave transition. *Phys. Rev. B* **52**, 5643–5652 (1995).

41. Wang, F. et al. Case for bulk nature of spectroscopic Luttinger liquid signatures observed in angle-resolved photoemission spectra of  $\text{Li}_{0.9}\text{Mo}_6\text{O}_{17}$ . *Phys. Rev. B* **74**, 113107 (2006).
42. Chudzinski, P., Jarlborg, T. & Giamarchi, T. Luttinger-liquid theory of purple bronze  $\text{Li}_{0.9}\text{Mo}_6\text{O}_{17}$  in the charge regime. *Phys. Rev. B* **86**, 075147 (2012).
43. Goodvin, G. L., Berciu, M. & Sawatzky, G. A. Green's function of the Holstein polaron. *Phys. Rev. B* **74**, 245104 (2006).
44. Yin, D. et al. Polarized Raman scattering study of blue bronze  $\text{Tl}_{0.3}\text{MoO}_3$ . *Phys. B: Condens. Matter* **405**, 3782–3786 (2010).
45. Richard Mortimer, James G. Powell, Martha Greenblatt, McCarroll WH, Ramanujachary AKV. Variable-temperature infrared spectroscopic study of some molybdenum bronzes: evidence for electron-phonon coupling. *J. Chem. Soc. Faraday Trans.* **89**, 3603–3609 (1993).
46. Lorenz, T. et al. Evidence for spin-charge separation in quasi-one-dimensional organic conductors. *Nature* **418**, 614–617 (2002).
47. Assaad, F. F. Spin, charge, and single-particle spectral functions of the one-dimensional quarter filled Holstein model. *Phys. Rev. B* **78**, 155124 (2008).
48. Ning, W.-Q., Zhao, H., Wu, C.-Q. & Lin, H.-Q. Phonon effects on spin-charge separation in one dimension. *Phys. Rev. Lett.* **96**, 156402 (2006).
49. Wang, J. et al. Growth of high quality and large-sized  $\text{Rb}_{0.3}\text{MoO}_3$  single crystals by molten salt electrolysis method. *J. Solid State Chem.* **178**, 1440–1444 (2005).
50. Kohn, W. & Sham, L. J. Self-consistent equations including exchange and correlation effects. *Phys. Rev.* **140**, A1133–A1138 (1965).
51. Giannozzi, P. et al. Advanced capabilities for materials modelling with quantum ESPRESSO. *J. Phys: Condens. Matter* **29**, 465901 (2017).
52. Giannozzi, P. et al. QUANTUM ESPRESSO: a modular and open-source software project for quantum simulations of materials. *J. Phys: Condens. Matter* **21**, 395502 (2009).
53. Perdew, J. P., Burke, K. & Ernzerhof, M. Generalized gradient approximation made simple. *Phys. Rev. Lett.* **77**, 3865–3868 (1996).
54. Pizzi, G. et al. Wannier90 as a community code: new features and applications. *J. Phys: Condens. Matter* **32**, 165902 (2020).

## Acknowledgements

The authors thank the helpful discussion with P.Z. Tang. This work was supported by the National Natural Science Foundation of China (Grants no. 11774190, no. 11427903, and no. 11634009), the National Key R&D program of China (Grants no. 2017YFA0304600, no. 2017YFA0305400, and no. 2017YFA0402900), and EPSRC Platform Grant (Grant no. EP/M020517/1).

## Author contributions

L.X.Y. and Y.L.C. conceived the experiments. L.K. and X.D. carried out ARPES measurements with the assistance of J.S.Z., X.G., Y.J.C., R.Z.X., Q.Q.Z., S.C.S., Z.X.Y., Y.W.L., D.P., J.Z., R.K.G., Z.G.W., Y.Z. and Z.K.L.; L.K. and X.D. performed the data analysis on the ARPES results; X.D. performed ab initio calculations; R.X. and J.S. synthesized the single crystals. Y.W.L. characterized the single crystals. L.K. and X.D. wrote the first draft of the paper. L.X.Y., Y.L.C. and J.S. contributed to the revision of the manuscript. All authors contributed to the scientific planning and discussion.

## Competing interests

The authors declare no competing interests.

## Additional information

**Supplementary information** The online version contains supplementary material available at <https://doi.org/10.1038/s41467-021-26078-1>.

**Correspondence** and requests for materials should be addressed to Y. L. Chen or L. X. Yang.

**Peer review information** *Nature Communications* thanks Jose Avila, and the other, anonymous, reviewer(s) for their contribution to the peer review of this work. Peer reviewer reports are available.

**Reprints and permission information** is available at <http://www.nature.com/reprints>

**Publisher's note** Springer Nature remains neutral with regard to jurisdictional claims in published maps and institutional affiliations.



**Open Access** This article is licensed under a Creative Commons Attribution 4.0 International License, which permits use, sharing, adaptation, distribution and reproduction in any medium or format, as long as you give appropriate credit to the original author(s) and the source, provide a link to the Creative Commons license, and indicate if changes were made. The images or other third party material in this article are included in the article's Creative Commons license, unless indicated otherwise in a credit line to the material. If material is not included in the article's Creative Commons license and your intended use is not permitted by statutory regulation or exceeds the permitted use, you will need to obtain permission directly from the copyright holder. To view a copy of this license, visit <http://creativecommons.org/licenses/by/4.0/>.

© The Author(s) 2021